Published in final edited form as:
Microporous Mesoporous Mater. ; 308: . doi:10.1016/j.micromeso.2020.110454.

Development and evaluation of copper-containing mesoporous bioactive glasses for bone defects therapy

J. Jiménez-Holguín[a], **S. Sánchez-Salcedo**[a,b,**], **M. Vallet-Regí**[a,b], **A.J. Salinas**[a,b,*]

[a]Dpt. Química en Ciencias Farmacéuticas, Facultad de Farmacia, Universidad Complutense de Madrid, UCM, Instituto de Investigación Hospital 12 de Octubre, imas12, 28040, Madrid, Spain

[b]Networking Research Center on Bioengineering, Biomaterials and Nanomedicine, CIBER-BBN, 28040, Madrid, Spain

Abstract

Mesoporous bioactive glasses (MBGs) are gaining increasing interest in the design of new biomaterials for bone defects treatment. An important research trend to enhance their biological behavior is the inclusion of moderate amounts of oxides with therapeutical action such as CuO. MBGs with composition (85-x)SiO_2-10-CaO–5P_2O_5–xCuO (x = 0, 2.5 or 5 mol-%) were synthesized, investigating the influence of the CuO content and some synthesis parameters in their properties. Two series were developed; first one used HCl as catalyst and chlorides as CaO and CuO precursors, second one, used HNO_3 and nitrates. MBGs of chlorides family exhibited calcium/copper phosphate nanoparticles between 10 and 20 nm in size. Nevertheless, CuO-containing MBGs of nitrates family showed metallic copper nanoparticles larger than 50 nm as well as quicker in vitro bioactive responses. Thus, MBGs of the nitrate series were coated by an apatite-like layer after 24 h soaked in simulated body fluid (SBF) a remarkably short period for a MBG containing 5% of CuO. A model, focused in the location of copper in the glass network, was proposed to relate nanostructure and in vitro behaviour. Moreover, after 24 h soaked in MEM or THB culture media, all the MBGs released therapeutic amounts of Ca^{2+} and Cu^{2+} ions. Because the quick bioactive response in SBF, the capacity to host biomolecules in their pores and to release therapeutic concentrations of Ca^{2+} and Cu^{2+} ions, MBGs of the nitrate families are proposed as excellent biomaterials for bone regeneration.

Keywords

Mesoporous bioactive glasses; CuO; Mesostructure; In vitro bioactivity; Therapeutic ions release

*Corresponding author. Dpt. Química en Ciencias Farmacéuticas, Facultad de Farmacia, Universidad Complutense de Madrid, UCM, Instituto de Investigación Hospital 12 de Octubre, imas12, 28040, Madrid, Spain. **Corresponding author. Dpt. Química en Ciencias Farmacéuticas, Facultad de Farmacia, Universidad Complutense de Madrid, UCM, Instituto de Investigación Hospital 12 de Octubre, imas12, 28040, Madrid, Spain. sansanch@ucm.es (S. Sánchez-Salcedo); salinas@ucm.es (A.J. Salinas).

CRediT authorship contribution statement

J. Jiménez-Holguín: Investigation, Data curation, Writing - original draft. **S. Sánchez-Salcedo:** Conceptualization, Methodology, Writing - original draft. **M. Vallet-Regí:** Resources, Supervision, Funding acquisition. **A.J. Salinas:** Conceptualization, Writing - review & editing, Supervision, Funding acquisition.

Declaration of competing interest

The authors declare that they have no known competing financial interests or personal relationships that could have appeared to influence the work reported in this paper.

Europe PMC Funders Author Manuscripts

1 Introduction

Mesoporous bioactive glasses, MBGs, of the SiO_2–CaO–P_2O_5 system are being widely investigated for bone diseases therapy, due to their amazing properties including ordered mesopores arrangements, narrow pore size distribution and huge surface areas and pore volumes [1–3]. MBGs belong to the family of bioactive glasses that have attracted much attention because of their capability to bond with bone and to stimulate osteogenesis and angiogenesis [4–7]. The reactivity of bioactive glasses in the biological environment begins with the ionic interchange of ions in the glass and protons from medium. A silica-rich layer is formed in the glass surface that attracts Ca^{2+} and P(V) ions from medium producing an amorphous calcium phosphate layer that, after crystallizing into bone-like carbonate apatite, plays an important role in the bond of bioactive glasses to bone [8]. These physical-chemical processes are speeded by the huge textural properties of MBGs. Moreover, these glasses are able to host molecules with biological activity inside their mesopores.

In the last years, several strategies were proposed to improve MBGs by loading with small biomolecules and drugs and/or oxides of chemical elements with biological activities such as copper [9–12]. It must be considered that copper is an essential trace element that account between 1.5 and 2.1 mg per kg of human body [13]. Many studies demonstrated that copper lack produces a loss of bone mineral density [14,15]. This was explained by the loss of activity of Cu-containing enzymes, like superoxide dismutase with antioxidant properties or lysyl oxidase, involved in the collagen cross-linking during the bone formation [16,17]. Furthermore, it is known the role of copper mimicking a hypoxia situation by stabilizing hypoxia inducible factor-1α (HIF-1α) expression. This situation increases the transcription of hypoxia sensitive genes, like vascular endothelial growth factor (VEGF) the proliferation of endothelial cells and the recruitment and differentiation of mesenchymal cells [18–22]. In addition, copper shows antibacterial behaviour against *E. coli*, *B. subtilis*, *S. aureus* [23–25], and antiviral activity against norovirus [26] and influenza A virus [27].

A recent paper Romero-Sanchez et al. reported the in vitro and in vivo angiogenic capability of SiO_2–CaO–P_2O_5 MBGs before and after doping with 5% of CuO [28]. On the other hand, in a previous article of our group, the synthesis conditions were adjusted to obtain copper-free MBGs composites showing nanometric calcium phosphate nuclei in the glass walls [29]. These nanocomposites maintained the structural properties of MBGs with enhanced in vitro reactivity in simulated body fluid, SBF due to the presence of mentioned apatite-like nuclei. The presence of the new-formed nanoapatite layer was detected after 24 h of immersion.

The starting point of the present study was to obtain MBGs with enhanced biological properties by the inclusion in their composition of 2.5 or 5 mol-% of CuO. Nevertheless, our previous studies demonstrated that the inclusion of a fourth oxide in ternary SiO_2–CaO–P_2O_5 MBGs produced a decrease in the in vitro bioactive response in SBF [30]. For this reason, a revision and reinvention of the method of synthesis used by Cicuendez et al. for copper-free MBGs [29] was here proposed for the synthesis of SiO_2–CaO–P_2O_5–CuO MBGs. Cicuendez et al. used hydrochloric acid and the chloride precursors of CaO for the synthesis of the nanocomposites because of the easy removal of chloride anions

by calcination. Accordingly, we investigated a family of CuO-MBGs, synthesized in the presence of hydrochloric acid and chlorides (Cu_HCl). However, most research groups more often use nitric acid and nitrates as sources for the MBGs syntheses [31–34]. Thus, another series of CuO-MBGs, was investigated employing nitric acid as catalyst and nitrates as CaO and CuO sources (Cu_HNO_3).

In this study, two families of MBGs, Cu_HCl and Cu_HNO_3, containing 0, 2.5 or 5 mol-% of CuO will be investigated. A detailed study of the MBGs nanostructure and also the in vitro behavior in SBF and in frequent culture media of cells and bacteria will be carried out. Our goal will be to relate the in vitro behavior of MBGs with their nanostructure and to determine if some of the MBGs designed could be of interest as bone substitute.

2 Experimental

2.1 Synthesis of the mesoporous bioactive glasses

Two families of MBGs with composition (85-x) SiO_2–CaO–P_2O_5–xCuO, (x = 0, 2.5 and 5) were synthesized by the Evaporation-Induced Self Assembly (EISA) method. First series, used HNO_3 1 M as catalyst and $Ca(NO_3)_2$•$4H_2O$ and $Cu(NO_3)_2$•$2.5H_2O$ as CaO and CuO sources. Second one was obtained using HCl 1 M, $CaCl_2$•$2H_2O$ and $CuCl_2$ as catalyst and sources of CaO and CuO. In all cases SiO_2 and P_2O_5 sources were tetraethyl orthosilicate (TEOS) and triethyl phosphate (TEP), respectively. In brief, the synthesis was performed by mixing Pluronic® F127, ethanol (99.98%), distilled water and HNO_3 or HCl, in a flask that was covered with Parafilm® and kept 1 h under stirring. (Reactants were purchased from Sigma-Aldrich, St. Louis, MO, USA). The corresponding amounts of reactants were added in the sequence indicated in Table 1 with 60 min intervals. The mixture was kept 14 h at 40 °C under stirring. Then, the mixture was poured in open Petri dishes (27 mL/plate) and kept 4 d at 30 °C in a stove to evaporate water and ethanol formed in the hydrolysis of the alkoxides. Along this process the critical micellar concentration, cmc, of surfactant was reached which yield the formation of mesophases that guided the formation of an ordered mesostructure during the silica condensation. After that, the total drying produced dried gels precursors of the MBGs. Finally, MBGs as powders were obtained by heating the dried gels for 6 h at 700 °C (heating ramp of 1 °C/min) to remove the surfactant contained into the mesopores and grinding and sieving the resultant materials with a 40 μm mesh. The in vitro studies were performed in disks, 10 mm diameter, 1 mm height, obtained compacting 100 mg of MBG powders in a mould with 5 MPa of uniaxial pressure for 1 min.

2.2 Physicochemical characterization of samples

Samples were characterized by Small-Angle X-ray diffraction, SA-XRD, in a X'pert-MPD system (Eindhoven, The Netherlands) equipped with Cu Kα radiation in the 0.6 to 8° 2θ range; Thermogravimetric and Differential Thermal analysis (TG/DTA) in the 30 °C to 900 °C interval (air flow: 100 mL/min) in a Perkin Elmer Pyris Diamond system (Waltham, MA, USA), Fourier transformed infrared (FTIR) spectroscopy in a Thermo Scientific Nicolet iS10 apparatus (Waltham, MA, USA) equipped with a SMART Golden Gate attenuated total reflection ATR diffuse reflectance accessory and Transmission Electron Microscopy (TEM), in a JEM-2100 JEOL microscope operating at 200 kV (Tokyo, Japan). For TEM analysis,

samples were dispersed in ethanol, sonicated and deposited in a nickel grid coated with a holed polyvinyl-formaldehyde layer. Moreover, materials were characterized by nitrogen porosimetry using Micromeritics 3 Flex (Norcross, GA, USA). For these measurements, the samples were previously degassed 24 h at 120 °C under vacuum. Surface area, S_{BET}, was calculated by the Brunauer-Emmett-Teller (BET) method [35], and pore size distributions by the Barret–Joyner–Halenda (BJH) method [36]. Finally, MBG samples were analyzed by ^{29}Si and ^{31}P solid state single pulse magic angle spinning nuclear magnetic resonance (SP MAS-NMR) on a Bruker Avance AV-400WB spectrometer (Karlsruhe, Germany) equipped with a 4 mm zirconia rotor. Frequencies were set at 79.49 and 161.97 MHz for ^{29}Si and ^{31}P respectively and chemical shift values were referenced to tetramethylsilane, for ^{29}Si, and H_3PO_4, for ^{31}P. Time period between accumulations were 5 s, for ^{29}Si and 4 s, for ^{31}P, and the number of scans was 10,000. MNR spectra were fitted with OriginLab 7.0 software (OriginLab Corporation, MA, USA). The quality of spectra fitting was checked by comparing the concordance of experimental and calculated spectra.

2.3 In vitro studies in acellular solutions

The reactivity of MBGs was assessed under in vitro conditions in SBF to evaluate the in vitro bioactivity and in culture media of cells or bacteria to quantify the amount of inorganic ions released to medium.

2.3.1 Assays in SBF—The surface reactivity of the samples was assessed by following the formation of an apatite-like layer on the MBG disks surface after being immersed in SBF [37]. MBG disks were sterilized with 20 min of UV radiation (10 min/face) in a laminar flux cabinet and the SBF solution was filtered with a 0.22 μm filter to avoid bacterial contaminations. MBG disks were soaked for 8 h, 24 h, 3 d and 7 d in 30 mL of SBF at 37 °C and a pH of 7.4. SBF volume was the one fulfilling with the proportion $V_S = D_S/0{,}075$ (V_s the SBF volume in mL and D_S the geometric external area in cm^2 of the item investigated) that we always maintain constant in our studies [31]. Inside the assay container, the disks were maintained in a vertical position with a support constructed with platinum wire. Assays were performed with two replicas by time and a material-free container only with SBF that was used as control.

Apatite-like phase formation was assessed by wide angle XRD (WA-XRD, 2θ from 10 to 70°), FTIR spectroscopy and scanning electron microscopy and (SEM) in a JSM-7600F JEOL microscope (JEOL, Tokyo, Japan) coupled with an energy dispersive X ray spectroscopy (EDS) system (Oxford Instruments, Abingdom, UK).

2.3.2 Ions release from disks—Assays were performed by soaking the MBG disks in 2 mL of Eagle's minimal essential medium, MEM, with 0.5% of penicillin-streptomycin and, in parallel, in 2 mL of Todd Hewitt Broth, THB, (both from Sigma-Aldrich. St. Louis, MO, USA). These studies allowed exploring the ion release in a mammal cell culture medium, MEM, and in a bacterial culture medium, THB. Samples were collected at 8 h and 1, 2, 3, 4, 5 and 6 d. The accumulative concentration of Ca^{2+}, P(V) and Cu^{2+} in both medium was determined by inductively coupled plasma/optical spectrometry (ICP/OES) using an OPTIMA 3300 DV device (Perkin Elmer, Waltham, MA, USA). Two replicas

Europe PMC Funders Author Manuscripts

were used of each composition. Three measures were taken of each replica to do statistical analysis.

2.3.3 Statistical analysisStatistical analysis—Results were evaluated with nonparametric Kruskal-Wallis test and post-hoc Dunn's test. A probability value, p-value < 0.05 was considered significant.

3 Results and discussion

3.1 Glass powders characterization

MBG powders were characterized by TEM and SA-XRD to determine their nanostructure and check if the mesoporous structure was formed and by nitrogen adsorption to determine the textural properties. Moreover, they were characterized by EDS and by FTIR spectroscopy to determine the composition and confirm the complete removal of surfactant and other impurities during the calcination. Finally, ^{29}Si and ^{31}P NMR spectroscopy allowed the characterization of these species at atomic level which will allow understanding the glasses reactivity in aqueous solutions.

Fig. 1 depicts the TEM images and EDS spectra of the MBGs investigated. All the micrographs show the presence of ordered mesoporosity. It is remarkable to mention that whereas Cu_HNO_3 MBGs show highly ordered arrangements of mesoporous channels, Cu_HCl MBGs exhibit smaller mesopores order and the presence of curved channels. Furthermore, both series showed the presence of pseudo-spherical nanospheres that were of different size for each family. Thus, Cu_HCl MBGs exhibited abundant nanoparticles under 20 nm with composition calcium, phosphorous and oxygen, similar to the apatite nanoparticles described by our group in CuO-free MBGs [29]. However, in Cu_HNO_3 MBGs, fewer amount of nanoparticles but bigger in size was detected. More than 30 nanoparticles were measured in each case obtaining sizes of 59 ± 13 and 77 ± 36 nm for the samples containing respectively 2.5% and 5% of CuO. Table 2 shows the MBGs composition determined by EDS. A quite good agreement between the experimental values and the expected ones, considering the amounts of reactants used in the MBGs syntheses, was observed.

Fig. 2A and 2A' includes SA-XRD diffraction patterns of MBGs. As observed, both series of materials exhibited a sharp maximum at around 1.0° in 2Θ, typical of mesoporous order, that was assigned to the (10) reflection of a 2D p6mm hexagonal phase (Table 3). In addition, in Cu_HCl MBGs it can be observed a shoulder at around 1.5° in 2Θ that was assigned to the (10), (20) reflections [30]. Nevertheless, in Cu_HNO_3 family (10) and (20) reflections were less defined, suggesting lower mesoporous order for these samples. SA-XRD results agree with those observed by TEM showing that Cu_HCl samples exhibited higher mesoporous order than Cu_HNO_3 ones.

Fig. 2B and 2B′ show the nitrogen adsoption/desorption isotherms of MBG powders. As observed, in all cases they are type IV that is characteristic of mesoporous materials. However two different hysteresis cycles were observed. Thus, MBGs of Cu_HNO_3 family with 2.5% and 5% of CuO exhibited type H1 cycle of hysteresis, characteristic of materials

with cylindrical pore channels. In contrast, the CuO-free glass of the nitrate series and all the Cu_HCl glasses showed a cycle of hysteresis type H2 that is related with materials exhibiting pores with bottleneck shape [38]. In addition, Fig. 2C and 2C' showed pore diameter distribution of MBGs, centred in 6–6.5 nm for Cu_HNO_3 MBGs and in 8.5–9 nm for Cu_HCl MBGs.

Table 2 displays the textural properties of MBGs as powders and after be conformed into disks. As is observed, in CuO-free samples (0% Cu_HCl and 0% Cu_HNO_3), S_{BET} values were somewhat greater for the MBG of the nitrate family, but in CuO-containing MBGs the chloride samples showed higher S_{BET} values. If we focus in Cu_HNO_3 family, S_{BET} decreased from 301 to 261 m^2/g and pore volume from 0.41 to 0.35 cm^3/g when CuO increased from 0% to 5%. These results agree with reported for the copper addition to other MBG compositions [28,39–41]. Besides, pore diameter of Cu_HNO_3 samples slightly decreased from 6.7 to 6.1 nm when the CuO content increased. This was explained considering the segregation of the large metallic copper nanoparticles in this series which could hinder the mesopores structural order.

However, in Cu_HCl glasses when CuO increased from 0% to 5%, S_{BET} increased from 218 to 295 m^2/g and pore volume from 0.40 to 0.47 cm^3/g. This effect was explained considering that the formation of the numerous calcium/copper phosphate smaller nanoparticles decreased the proportion of network modifiers (Ca^{2+} and Cu^{2+}) in the MBG structure increasing the participation of the glass network forming (SiO_2) and therefore increases the order in the structure. Nevertheless, all Cu_HCl samples exhibited pore diameters around 8 nm, showing that CuO inclusions have not effects on the pore diameter of this family of MBGs. In summary, nitrogen adsorption results suggested that copper exerts a different effect in the textural properties of MBG depending on the catalyst and precursors used for the synthesis.

On the other hand, ^{29}Si and ^{31}P NMR measurements were carried out to investigate the environments at the atomic level of the network formers in the MBGs. Fig. 3 shows the ^{29}Si NMR spectra where Q^2, Q^3, and Q^4 represent three different environments of the silicon atom (Si*): $(NBO)_2Si^*–(OSi)_2$, $(NBO)Si^*–(OSi)_3$, and $Si^*(OSi)_4$ (NBO: non-bonding oxygen). Moreover, Table 4 includes the chemical shifts (CS), the area of the peaks, expressed as %, and the silica network connectivity $<Q^n>$ of each MBG. As is observed, the signals at −111 to −112 ppm were assigned to Q^4, at −102 to −106 ppm to Q^3 and at −95 to −98 ppm to Q^2 [42].

Fig. 4 shows the ^{31}P NMR spectra of MBGs, where Q^0 and Q^1 represent the phosphorus atom (P*) in the PO_4^{3-} species: $P^*–(NBO)_4$ and $(NBO)_3–P^*–(OP)$. The CS and the area of the peaks in % of P were also included in Table 4 where the intense signals in the range 1.8–2.2 ppm were assigned to the Q^0 environment typical of P in amorphous orthophosphate. For Cu_HNO_3 samples a second weak signal (Q^1), between −5.4 and −4.5 ppm, was observed which intensity increased as CuO in the MBG increased. This second maximum that is in the Q^1 tetrahedra range could be assigned to P–O–Si environments as previously reported [42]. This effect could suppose an incorporation of phosphorous in the glass network and consequently a decrease of amorphous orthophosphate clusters favouring the formation of

metallic copper nanoparticles observed by TEM (Fig. 1). The slight variation of the network connectivity when copper was added to nitrate MBGs demonstrated the segregation of Cu in metallic nanoparticles and no copper participation in the glass network.

In addition, the high values of Q^0 for Cu_HCl glasses, up to 91.7% and 90.4%, observed in Table 4, suggest that phosphorous would be mainly in these glasses as orthophosphate clusters decreasing the proportion of P–O–Si units. Besides, it is worthy to note that the introduction of copper in Cu_HCl samples caused a large decrease in the percentage of Q^1, from 29.9%, for CuO-free glass, to 8.3% and 9.1% respectively, for MBGs with 2.5 and 5% of CuO. This variation agrees with the decrease of the network connectivity when Cu^{2+} is incorporated to the glass structure [43], indicating that this ion act as a network modifier and favours the orthophosphate clusters formation that were observed by TEM (Fig. 1). Moreover, these results suggest that copper hinders phosphate groups to participate as network formers which will be affect the in vitro bioactive response of Cu_HCl MBGs.

Therefore, the differences observed in the Q^0-Q^1 balance of MBGs with 0% of CuO can be explained by the smaller integration of P in HNO_3 series in contrast to HCl series

As is observed in Table 2. HCl series showed nanoparticles of calcium phosphate in their structure as reported in analogous MBGs by Cicuéndez et al. [29]. On the other hand, copper behaves differently in each series, favouring the participation of P as network former in HNO_3 series, which accordingly exhibit higher Q^1 percentages. However, in HCl series phosphorus seems to participate in forming ortophos phate clusters which would agree with the higher values of Q^0 percentages in these MBGs.

3.2 Characterization of the MBG disks by nitrogen adsorption

Previous section describes the physical-chemical characterization of MBG powders. However, for the in vitro studies in SBF as well as in both MEM and THB culture media the powders were conformed into disks. In this section, the characterization of MBG disks by nitrogen adsorption is described to verify that the processing of powders did not modify significantly the textural properties. Fig. 5 shows the nitrogen adsorption/desorption isotherms and the pore diameter distributions of MBG disks. As is observed, the isotherms are analogous to those of MBG powders showed in Fig. 2. Moreover, Table 2 collects the textural parameters of both MBG powders and MBG disks. Values in Table 2 confirm that both series of MBG powders experience a small surface area decrease in their processing into disks, average 17% for Cu_HNO_3 glasses, and 3% for Cu_HCl samples. These decreases are consequence of the partial collapse of the pore structure of glasses due to the uniaxial pressure exerted to obtain the disks. However, the isotherms shape and the pore diameter size remain stable for both series of materials. Furthermore, S_{BET} and pore volume of MBG disks are in all cases much more than enough for the intended application of these materials in bone disease treatment.

3.3 In vitro bioactivity assays of the MBG disks in simulated body fluid

Two disks of each MBG composition were soaked in SBF for 8 h, 24 h, 3 d and 7 d. Disks were analyzed by FTIR spectroscopy (Figs. 6 and 7) and SEM-EDS (Fig. 8) before and after be immersed in SBF. FTIR spectra of MBGs before soaking in SBF showed asymmetric

bending vibration Si–O–Si bands at 1100-1040 cm^{-1} and 478-441 cm^{-1} and a band at 800-793 cm^{-1} of the symmetric Si–O stretch [31]. Moreover, the spectra of Cu_HNO_3 MBGs showed a very low intensity band at 590 cm^{-1} that was attributed to the presence to a phosphate phase with extremely small crystalline domain size, often denoted as amorphous calcium phosphate (a-CaP). However, the spectra of Cu_HCl samples exhibit in this region two small bands at about 600 and 570 cm^{-1} characteristic of phosphate in a crystalline environment. Such bands, visible before soaking the MBGs in SBF, were attributed by Cicuéndez et al. to the nanocrystalline apatite phases in their nanocomposites [29].

After soaking nitrate-based MBGs in SBF, bands at 600 and 570 cm^{-1} in the FTIR spectra were detected which intensity increased with soaking time. The presence of these bands of nanometric hydroxycarbonate apatite (n-HCA) in the assays in SBF is indicative of the in vitro bioactive response of a tested material [30]. After 8 h of soaking these bands were clearly visible in 0%Cu_HNO_3 and 2.5% Cu_HNO_3 spectra, although the intensity decreased when the CuO content increased. Thus, for 5%Cu_HNO_3, the mentioned bands were only visible after 24 h of assay in SBF. This delay in the n-HCA formation was explained considering that the high copper content in the MBG prevents a quicker bioactive response. The very short time for the in vitro bioactive response of the CuO-free glass is similar to reported by us and other research groups in equivalent ternary MBGs. However, 8 h to show in vitro bioactive response is a very short time for a MBG containing 2.5% of CuO.

On the other hand, MBG of the Cu_HCl series showed a more moderated in vitro bioactive response than Cu_HNO_3 glasses. However, all the glasses exhibited an in vitro bioactive response after 7 d or less in SBF. In some of the spectra of Cu_HCl MBGs after soaking in SBF is not clear about whether the two bands in this region come from the phosphate nuclei initially present in the MBG or of n-CHA formed after the in vitro bioactivity tests. Probably in several cases the bands observed are sum of the two types of bands mentioned. Therefore, another technique is necessary, i.e. SEM, which allowed checking in which cases the MBGs surface was coated by a newly formed material.

Fig. 8 shows the SEM images of MBG disks of the two series before and after soaking 8 and 24 h in SBF. For each sample, the corresponding EDS spectrum was also included, as well as the Ca/P molar ratio. The images of MGB disks before soaking show the bare surface of disks, where the grains of MBG powders used to obtain the disks are still visible. However, after 8 h of soaking, the surface of more reactive samples is coated by a newly formed layer, whereas the surface of other samples remained unchanged. At 24 h, all the disks are coated by a newly formed layer indicative of an in vitro bioactive response.

Several steps can be distinguished in the formation in SBF of the layer that is indicative of the in vitro bioactive response of a material. These steps are related with the in vivo mineralization process [44–46]. The process starts with the formation of a smooth layer of a-CaP coating the disks. The layer evolves into needle-like nanocrystals of n-CHA. Finally, the thickness of the layer increases until a certain maximum value. Checking in which phase is each sample at each time, comparative information between the bioactive responses of MBGs can be obtained.

Indeed, in the biomineralization process in the maturation of a-CaP to n-CHA an intermediate phase of octacalcium phosphate (OCP) is formed. OCP was only detected in vitro for MBG compositions of with an especially quick bioactive response. Detect OCP formation is a rather complex procedure that requires High Resolution TEM (HR-TEM) analysis. Once our group detected the in vitro formation of OCP in some MBGs, this was not a priority o of this study. However, our experience allows predicting that, at least in the CuO-free MBG of nitrate series, OCP will be formed in the in vitro assays.

As is observed in Fig. 8, at 8 h the a-CaP layer was formed on 2.5% and 5%_HNO_3 samples. However, at this time the bioactive response 0%_HNO_3 was more advanced because the needle-like n-CHA layer was already formed. Regarding the Cu_HCl series, a-CaP formation was not observed at 8 h indicating the slower bioactive response of this series compared with nitrates one. However, a layer was present in the three cases after 24 h, again the CuO-free MBG was the one with a quicker bioactive response because the needle-like particles of n-CHA were observed.

After 24 h in SBF, surface of Cu_HNO_3 MBGs with 2.5% and 5% of CuO were coated with the thick n-CHA layer that was observed at 8 h for the CuO-free sample. Nevertheless, in the Cu_HCl series this thick layer was only observed after 24 h of treatment for the Cu-free sample. In the samples with 2.5% and 5% of CuO, the layer formed at 24 h was thinner and did not totally coat the surface of disks, evidencing that these samples exhibit lower in vitro bioactive response than Cu_HNO_3 series.

SEM results agree with obtained by FTIR (Figs. 6 and 7) where it was monitored the presence of: a band at 590 cm^{-1}, indicative of a-CaP, two bands at 570 and 600 cm^{-1} of n-CHA, and the increasing in the intensity of the bands when the layer thickness increased..

In summary, two general trends were observed regarding the in vitro response of MBGs: for the same composition, nitrate-based MBGs exhibited quicker bioactive response than chloride series, and for both series, the bioactive response decreased when copper amount in the MBG increased.

As it was observed in the previous paragraphs, SBF is a solution especially suitable for forming the n-CHA layer and consequently is excellent for comparative bioactivity screening here performed. However, SBF composition, without biochemical components, is far from the MBGs body conditions when implanted, but is also far from the solutions were the next steps in the MBGs assessment will be performed. Indeed, MBGs here optimized will be investigated in cell cultures to verify their osteogenic and angiogenic properties and in bacterial studies to evaluate their bactericidal capacity. For this reason, release studies of ions from MBGs were performed in cultures media of mammal cells, such as MEM, and of bacteria, such as THB.

Figs. 9 and 10 show the cumulative Ca, Cu and P ions release from both MBG series in MEM and THB culture media up to 6 d. Taking into account that MEM contains 90% more Ca and 50% less P in its composition than THB, absolute values between both media are not comparable. Results of Cu_HNO_3 series are depicted on Fig. 9, and show ions release profiles of Ca and P typical of highly bioactive glasses followed by

release-precipitation equilibrium. In THB the three nitrate-based MBGs released analogous Ca amounts, being higher for CuO-free MBG after 3 d for both media and significantly different in MEM, reaching 102 ppm for Cu-free sample (Fig. 9). Regarding Cu ions (Fig. 9), knowing that copper are imbibed in glass structure as metallic nanoparticles (Figs. 1 and 3), higher amount of Cu nanoparticles in MBGs increase the release to the medium as it can be observed in MEM, being the difference between 2.5% Cu_HNO_3 and 5% Cu_HNO_3 samples up to 300 ppm after 6 d of treatment. However, it was inversely proportional due to the precipitation of copper phosphate when the cooper in medium is increased in THB (Fig. 9) [30].

The same assay was performed for chloride series (Fig. 10). Since Cu_ HCl series stands out for having a high content of Ca/CuP nanoparticles imbibed in their structure (Fig. 1) and copper ions as a network modifier as it have been demonstrated by NMR (Fig. 3, Table 4). Ca and P ions (Fig. 10) release are typical of bioactive glasses followed the release-precipitation equilibrium. Moreover, there was a significantly deference between CuO-free samples and MBGs doped with Cu due to the different bioactive kinetic that has been demonstrated in the bioactive behaviour of this chloride-based series (Fig. 8) being more bioactive the CuO-free MBGs. In case of Cu ion (Fig. 10) release when copper enrichment are higher in the Cu_HCl series the amount of Cu released are significantly increased in both cell and bacteria media with a difference up to 150 and 600 ppm in MEM and THB, respectively. This effect confirms the decrease network connectivity (Q^n) calculated in NMR (Table 4) when Cu are increased in the MBG structure and thus more soluble in aqueous media.

The MBGs containing 2.5% and 5% of CuO investigated released therapeutic concentration of Cu^{2+} ions in MEM at 24 h with increments for each time in the cytocompatibility range [2]. However, after 6 d in THB, they released larger amounts of Cu^{2+} than in MEM. Consequently, CuO-containing MBGs here investigated, exhibiting good in vitro bioactivity and Cu^{2+} release capability can be proposed for therapeutical application against bacterial infection. However, inclusion in the MBGs smaller than 2.5% of CuO will be investigated to ensure their cytocompatibility along with their antibacterial properties.

Conclusions

Two series of mesoporous bioactive glasses with composition (85-x)SiO_2–10CaO–5P_2O_5–xCuO (x = 0, 2.5%, 5 mol-%) were obtained by using nitrate or chloride precursors in their syntheses. Nanostructure and in vitro behaviour of MBGs were dependent on the synthesis conditions. CuO additions exerted different effect in the textural properties of MBGs of each series. However, all the MBGs showed high pore volumes and specific surface areas. Moreover, MBGs exhibited highly ordered mesoporous nanostructures and calcium/copper phosphate nanoparticles (10–20 nm) in Cu_HCl series, and nanoparticles larger than 50 nm of metallic copper in Cu_HNO_3 family.

The different nanostructures of MBGs yielded to diverse in vitro behaviours in simulated body fluid (SBF) or in cell (MEM) and bacteria (THB) culture media. Different location of copper in the glass structure for each series allowed explaining their different in vitro

Europe PMC Funders Author Manuscripts

behaviours. MBGs released therapeutic amounts of Ca^{2+} and Cu^{2+} ions at 24 h. Moreover, MBGs of nitrate series exhibited quicker in vitro bioactive responses. Thus, MBG with 2.5% of CuO was coated by an apatite layer after 24 h in SBF, a remarkably short period for a MBG with this amount of CuO. Because of the quick bioactive response in SBF, the capacity to release therapeutic concentrations of ions and to host biomolecules, MBGs of the nitrate series are proposed as biomaterials for bone regeneration, and deserve further in vitro and in vivo studies.

Acknowledgements

This study was supported by research grants from Instituto de Salud Carlos III (PI15/00978) project co-financed with the European Union FEDER funds, the European Research Council (ERC-2015-AdG), Advanced Grant Verdi-Proposal No.694160 and Youth Employment initiative (YEI) from Comunidad de Madrid (PEJ-2017-2017-AI/SALl-5825).

References

[1]. Izquierdo-Barba I, Salinas AJ, Vallet-Regí M. Bioactive glasses: from macro to nano. Int J Appl Glass Sci. 2013; 4: 149–161. DOI: 10.1111/ijag.12028

[2]. Wu C, Chang J. Multifunctional mesoporous bioactive glasses for effective delivery of therapeutic ions and drug/growth factors. J Contr Release. 2014; 193: 282–295. DOI: 10.1016/j.jconrel.2014.04.026

[3]. Yan X, Yu C, Zhou X, Tang J, Zhao D. Highly ordered mesoporous bioactive glasses with superior in vitro bone-forming bioactivities. Angew Chem Int Ed. 2004; 43: 5980–5984. DOI: 10.1002/anie.200460598

[4]. Hench LL. The story of Bioglass®. J Mater Sci Mater Med. 2006; 17: 967–978. DOI: 10.1007/s10856-006-0432-z [PubMed: 17122907]

[5]. Hench LL. Genetic design of bioactive glass. J Eur Ceram Soc. 2009; 29: 1257–1265. DOI: 10.1016/j.jeurceramsoc.2008.08.002

[6]. Gorustovich AA, Roether JA, Boccaccini AR. Effect of bioactive glasses on angiogenesis: a review of in vitro and in vivo evidences. Tissue Eng B Rev. 2010; 16: 199–207. DOI: 10.1089/ten.teb.2009.0416

[7]. Hench LL, Polak JM. Third-generation biomedical materials. Science. 2002; 295: 1014–1017. DOI: 10.1126/science.1067404 [PubMed: 11834817]

[8]. Salinas AJ, Vallet-Regí M. Bioactive ceramics: from bone grafts to tissue engineering. RSC Adv. 2013; 3: 11116–11131. DOI: 10.1039/c3ra00166k

[9]. Gupta N, Santhiya D. Mesoporous Bioactive Glass and its Applications. Bioact Glas. 2018; 63–85. DOI: 10.1016/b978-0-08-100936-9.00003-4

[10]. Koohkan R, Hooshmand T, Tahriri M, Mohebbi-Kalhori D. Synthesis, characterization and in vitro bioactivity of mesoporous copper silicate bioactive glasses. Ceram Int. 2018; 44: 2390–2399. DOI: 10.1016/J.CERAMINT.2017.10.208

[11]. Li J, Zhai D, Lv F, Yu Q, Ma H, Yin J, Yi Z, Liu M, Chang J, Wu C. Preparation of copper-containing bioactive glass/eggshell membrane nanocomposites for improving angiogenesis, antibacterial activity and wound healing. Acta Biomater. 2016; 36: 254–266. DOI: 10.1016/J.ACTBIO.2016.03.011 [PubMed: 26965395]

[12]. Baino F, Potestio I, Vitale-Brovarone C. Production and physicochemical characterization of Cu-doped silicate bioceramic scaffolds. Mater (Basel, Switzerland). 2018; 11: 1524. doi: 10.3390/ma11091524

[13]. Borkow G, Gabbay J. Copper as a biocidal tool. Curr Med Chem. 2005; 12: 2163–2175. DOI: 10.2174/0929867054637617 [PubMed: 16101497]

[14]. Jonas J, Burns J, Abel EW, Cresswell MJ, Strain JJ, Paterson CR. Impaired mechanical strength of bone in experimental copper deficiency. Ann Nutr Metab. 1993; 37: 245–252. DOI: 10.1159/000177774 [PubMed: 8311418]

Europe PMC Funders Author Manuscripts

[15]. Smith BJ, King JB, Lucas EA, Akhter MP, Arjmandi BH, Stoecker BJ. Nutrient metabolism skeletal unloading and dietary copper depletion are detrimental to bone quality of mature rats. J Nutr. 2002; 132: 190–196. DOI: 10.1093/jn/132.2.190 [PubMed: 11823577]

[16]. Nojiri H, Saita Y, Morikawa D, Kobayashi K, Tsuda C, Miyazaki T, Saito M, Marumo K, Yonezawa I, Kaneko K, Shirasawa T, et al. Cytoplasmic superoxide causes bone fragility owing to low-turnover osteoporosis and impaired collagen cross-linking. J Bone Miner Res. 2011; 26: 2682–2694. DOI: 10.1002/jbmr.489 [PubMed: 22025246]

[17]. Opsahl W, Zeronian H, Ellison M, Lewis D, Rucker RB, Riggins RS. Role of copper in collagen cross-linking and its influence on selected mechanical properties of chick bone and tendon. J Nutr. 1982; 112: 708–716. DOI: 10.1093/jn/112.4.708 [PubMed: 6121843]

[18]. Finney L, Vogt S, Fukai T, Glesne D. Copper and angiogenesis: unravelling a relationship key to cancer progression. Clin Exp Pharmacol Physiol. 2009; 36: 88–94. DOI: 10.1111/j.1440-1681.2008.04969.x [PubMed: 18505439]

[19]. Gérard C, Bordeleau L-J, Barralet J, Doillon CJ. The stimulation of angiogenesis and collagen deposition by copper. Biomaterials. 2010; 31: 824–831. DOI: 10.1016/j.biomaterials.2009.10.009 [PubMed: 19854506]

[20]. Sen CK, Khanna S, Venojarvi M, Trikha P, Ellison EC, Hunt TK, Roy S. Copper-induced vascular endothelial growth factor expression and wound healing. Am J Physiol Cell Physiol. 2002; 282: 1821–1827. DOI: 10.1152/ajpheart.01015.2001

[21]. Hu G. Copper stimulates proliferation of human endothelial cells under culture. J Cell Biochem. 1998; 69: 326–335. DOI: 10.1002/(SICI)1097-4644(19980601)69:3<326::AID-JCB10>3.0.CO;2-A [PubMed: 9581871]

[22]. Rath SN, Brandl A, Hiller D, Hoppe A, Gbureck U, Horch RE, Boccaccini AR, Kneser U. Bioactive copper-doped glass scaffolds can stimulate endothelial cells in co-culture in combination with mesenchymal stem cells. PloS One. 2014; 9 doi: 10.1371/journal.pone.0113319

[23]. Ye J, He J, Wang C, Yao K, Gou Z. Copper-containing mesoporous bioactive glass coatings on orbital implants for improving drug delivery capacity and antibacterial activity. Biotechnol Lett. 2014; 36: 961–968. DOI: 10.1007/s10529-014-1465-x [PubMed: 24563298]

[24]. Ruparelia JP, Chatterjee AK, Duttagupta SP, Mukherji S. Strain specificity in antimicrobial activity of silver and copper nanoparticles. Acta Biomater. 2008; 4: 707–716. DOI: 10.1016/J.ACTBIO.2007.11.006 [PubMed: 18248860]

[25]. Yoon K-Y, Hoon Byeon J, Park J-H, Hwang J. Susceptibility constants of *Escherichia coli* and *Bacillus subtilis* to silver and copper nanoparticles. Sci Total Environ. 2007; 373: 572–575. DOI: 10.1016/J.SCITOTENV.2006.11.007 [PubMed: 17173953]

[26]. Barker J, Vipond IB, Bloomfield SF. Effects of cleaning and disinfection in reducing the spread of Norovirus contamination via environmental surfaces. J Hosp Infect. 2004; 58: 42–49. DOI: 10.1016/J.JHIN.2004.04.021 [PubMed: 15350713]

[27]. Noyce JO, Michels H, Keevil CW. Inactivation of influenza A virus on copper versus stainless steel surfaces. Appl Environ Microbiol. 2007; 73: 2748. doi: 10.1128/AEM.01139-06 [PubMed: 17259354]

[28]. Romero-Sánchez LB, Marí-Beffa M, Carrillo P, Medina MÁ, Díaz-Cuenca A. Copper-containing mesoporous bioactive glass promotes angiogenesis in an in vivo zebrafish model. Acta Biomater. 2018; 68: 272–285. DOI: 10.1016/J.ACTBIO.2017.12.032 [PubMed: 29288822]

[29]. Cicuéndez M, Portolés MT, Izquierdo-Barba I, Vallet-Regí M. New nanocomposite system with nanocrystalline apatite embedded into mesoporous bioactive glass. Chem Mater. 2012; 24: 1100–1106. DOI: 10.1021/cm203416x

[30]. Shruti S, Salinas AJ, Lusvardi G, Malavasi G, Menabue L, Vallet-Regi M. Mesoporous bioactive scaffolds prepared with cerium-, gallium- and zinc-containing glasses. Acta Biomater. 2013; 9: 4836–4844. DOI: 10.1016/j.actbio.2012.09.024 [PubMed: 23026489]

[31]. Heras C, Sanchez-Salcedo S, Lozano D, Peña J, Esbrit P, Vallet-Regi M, Salinas AJ. Osteostatin potentiates the bioactivity of mesoporous glass scaffolds containing Zn^{2+} ions in human mesenchymal stem cells. Acta Biomater. 2019; 89: 359–371. DOI: 10.1016/J.ACTBIO.2019.03.033 [PubMed: 30890462]

[32]. Zhao S, Zhang J, Zhu M, Zhang Y, Liu Z, Tao C, Zhu Y, Zhang C. Acta Biomaterialia Three-dimensional printed strontium-containing mesoporous bioactive glass scaffolds for repairing rat critical-sized calvarial defects. Acta Biomater. 2015; 12: 270–280. DOI: 10.1016/j.actbio.2014.10.015 [PubMed: 25449915]

[33]. Xia W, Chang J. Well-ordered mesoporous bioactive glasses (MBG), A promising bioactive drug delivery system. 2006; 110: 522–530. DOI: 10.1016/j.jconrel.2005.11.002

[34]. Philippart A, Gómez-Cerezo N, Arcos D, Salinas AJ, Boccardi E, Vallet-Regi M, Boccaccini AR. Novel ion-doped mesoporous glasses for bone tissue engineering: study of their structural characteristics influenced by the presence of phosphorous oxide. J Non-Cryst Solids. 2017; 455: 90–97. DOI: 10.1016/j.jnoncrysol.2016.10.031

[35]. Brunauer S, Emmett PH, Teller E. Adsorption of gases in multimolecular layers. J Am Chem Soc. 1938; 60: 309–319. DOI: 10.1021/ja01269a023

[36]. Barrett EP, Joyner LG, Halenda PP. The determination of pore volume and area distributions in porous substances. I. Computations from nitrogen isotherms. J Am Chem Soc. 1951; 73: 373–380. DOI: 10.1021/ja01145a126

[37]. Salinas AJ, Vallet-Regí M. Glasses in bone regeneration: a multiscale issue. J Non-Cryst Solids. 2016; 432: 9–14. DOI: 10.1016/J.JNONCRYSOL.2015.03.025

[38]. ALOthman Z. A review: fundamental aspects of silicate mesoporous materials, Materials. 2012; 5: 2874–2902. DOI: 10.3390/ma5122874

[39]. Wang X, Cheng F, Liu J, Smått JH, Gepperth D, Lastusaari M, Xu C, Hupa L. Biocomposites of copper-containing mesoporous bioactive glass and nanofibrillated cellulose: biocompatibility and angiogenic promotion in chronic wound healing application. Acta Biomater. 2016; 46: 286–298. DOI: 10.1016/j.actbio.2016.09.021 [PubMed: 27646503]

[40]. Luo H, Xiao J, Peng M, Zhang Q, Yang Z, Si H, Wan Y. One-pot synthesis of copper-doped mesoporous bioglass towards multifunctional 3D nanofibrous scaffolds for bone regeneration. J Non-Cryst Solids. 2020; 532 doi: 10.1016/j.jnoncrysol.2019.119856

[41]. Wang C, Jin K, He J, Wang J, Yang X, Yao C, Dai X, Gao C, Gou Z, Ye J. Synergistic effect of copper-containing mesoporous bioactive glass coating on stimulating vascularization of porous hydroxyapatite orbital implants in rabbits. J Biomed Nanotechnol. 2018; 14: 688–697. DOI: 10.1166/jbn.2018.2513 [PubMed: 31352942]

[42]. Leonova E, Izquierdo-Barba I, Arcos D, López-Noriega A, Hedin N, Vallet-Regí M, Edén M. Multinuclear Solid-State NMR Studies of Ordered Mesoporous Bioactive Glasses. 2008; 112: 5552–5562. DOI: 10.1021/jp7107973

[43]. Ben–Arfa BAE, Neto S, Miranda Salvado IM, Pullar RC, Ferreira JMF. Robocasting of Cu^{2+} & La^{3+} doped sol–gel glass scaffolds with greatly enhanced mechanical properties: compressive strength up to 14 MPa. Acta Biomater. 2019; 87: 265–272. DOI: 10.1016/J.ACTBIO.2019.01.048 [PubMed: 30690209]

[44]. Kokubo T, Takadama H. How useful is SBF in predicting in vivo bone bioactivity? Biomaterials. 2006; 27: 2907–2915. DOI: 10.1016/j.biomaterials.2006.01.017 [PubMed: 16448693]

[45]. Mathew R, Turdean-Ionescu C, Yu Y, Stevensson B, Izquierdo-Barba I, García A, Arcos D, Vallet-Regí M, Edén M. Proton environments in biomimetic calcium phosphates formed from mesoporous bioactive CaO-SiO_2-P_2O_5 glasses in vitro: insights from solid-state NMR. J Phys Chem C. 2017; 121: 13223–13238. DOI: 10.1021/acs.jpcc.7b03469

[46]. Ye D, Tang W, Xu Z, Zhao X, Wang G. Application of MBG as a coating material on mechanically stronger but less degradable ceramic scaffolds for enhanced osteogenesis. Mater Lett. 2018; 223: 105–108. DOI: 10.1016/j.matlet.2018.03.202

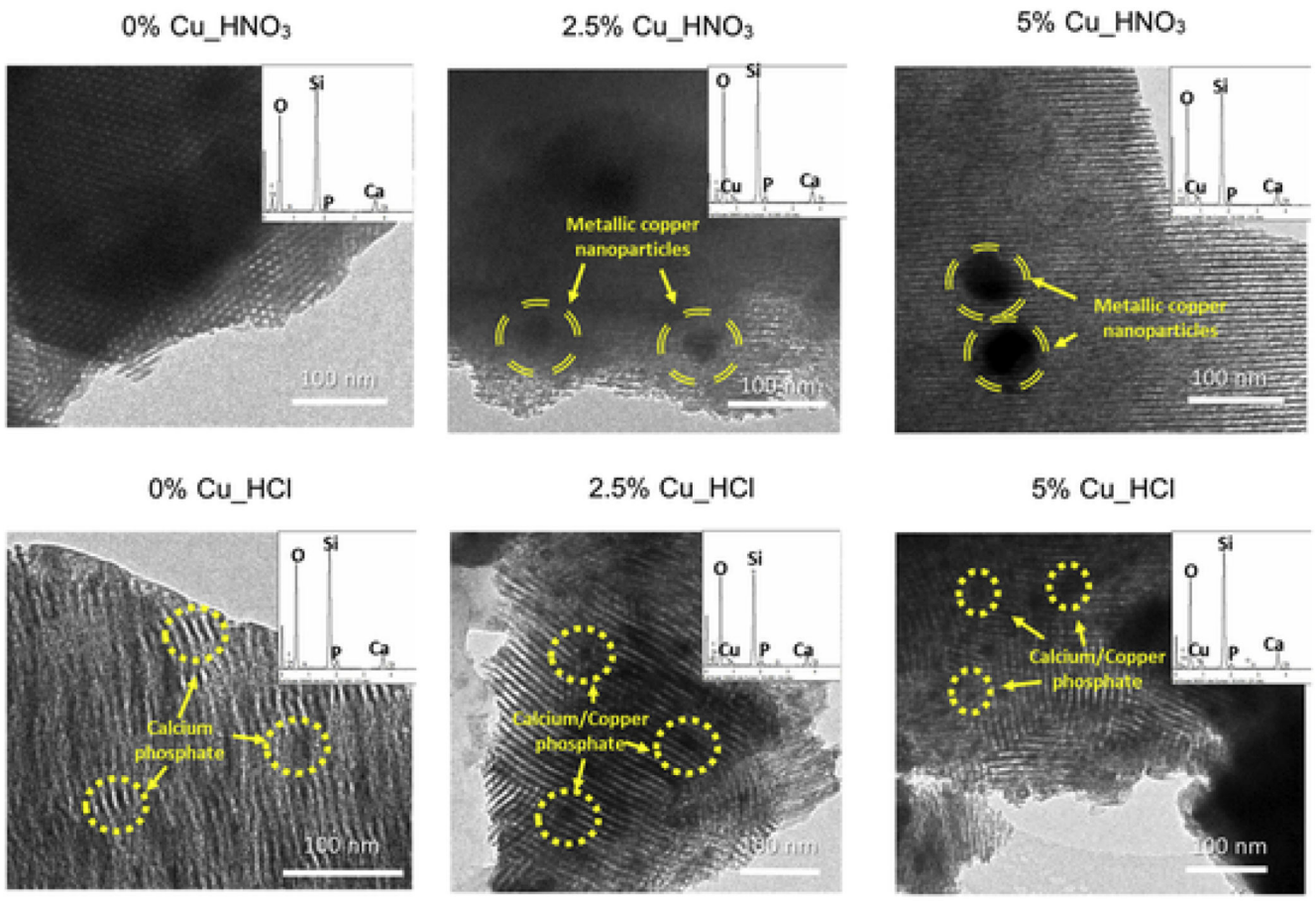

Fig. 1.

TEM images of the two series of MBGs enriched with 0, 2.5 and 5% of CuO synthetized by using HNO_3/nitrate or HCl/chloride. Highlighted with striped circles the metallic copper nanoparticles and with dotted circles those of calcium/copper phosphate. Each image includes in the up right corner their EDS espectrum.

Europe PMC Funders Author Manuscripts

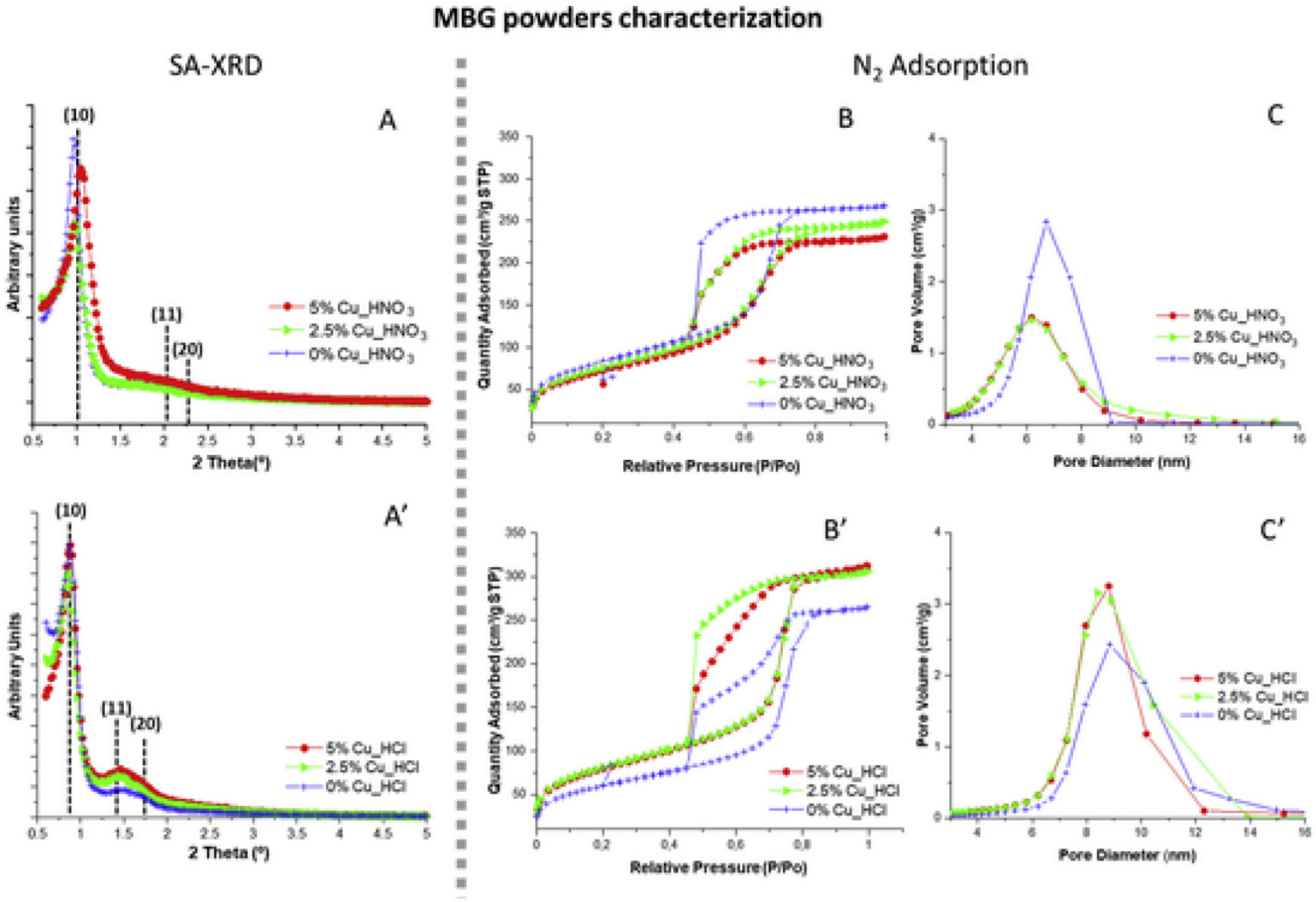

Fig. 2.

Left, SA-XRD patterns of MBGs synthesized in the presence of HNO_3/nitrate or HCl/chloride (A, A′). Right, N_2-adsorption results showing the isotherms (B, B′) and pore size distributions (C, C′) of both MBG series.

Europe PMC Funders Author Manuscripts

Europe PMC Funders Author Manuscripts

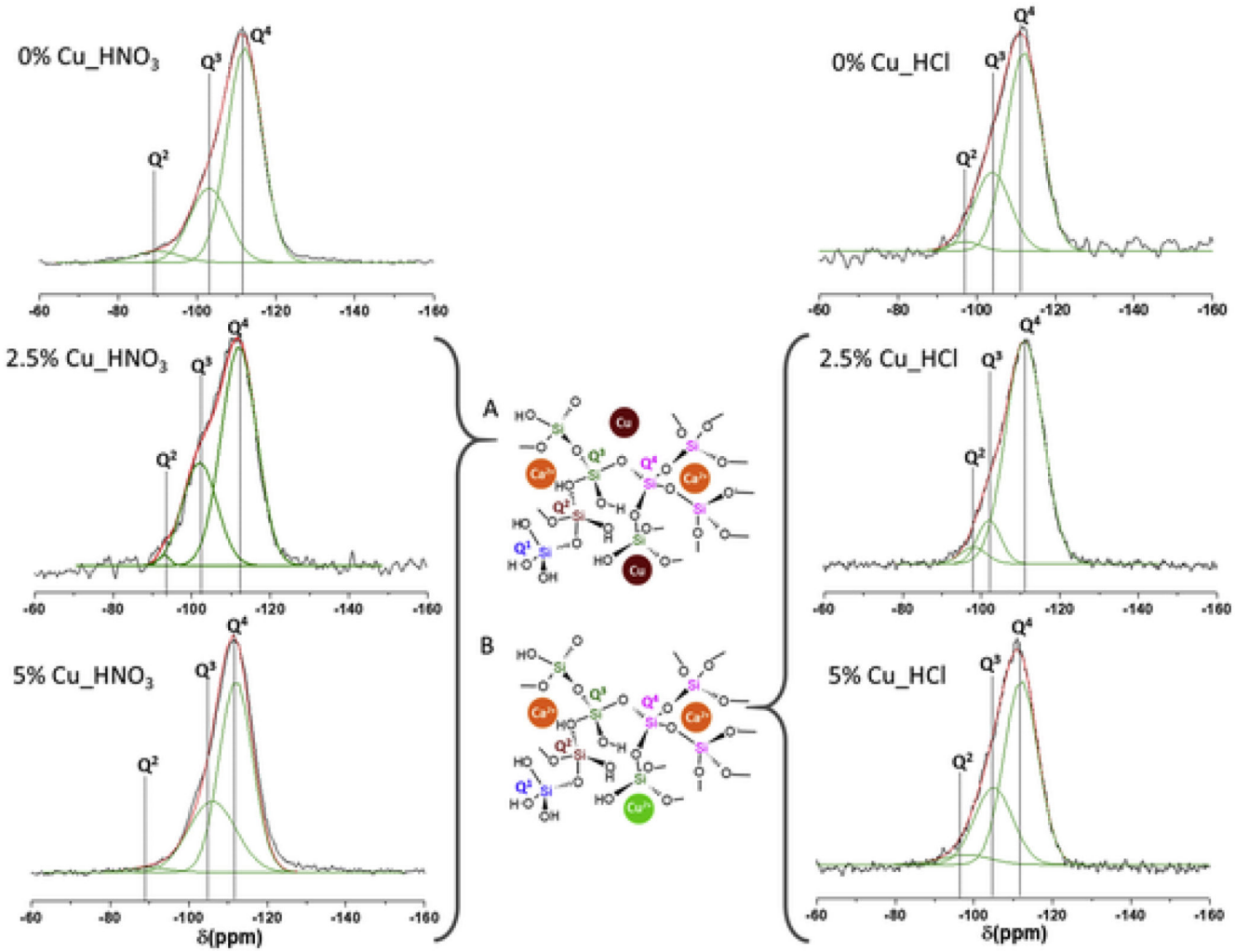

Fig. 3.

Solid-state ^{29}Si single-pulse MAS-NMR spectra of MBGs. Q^2, Q^3 and Q^4, obtained by Gaussian line-shape deconvolution, are displayed in green. Left: nitrate series. Right: chloride series. Two models showing the copper location in the glass network were proposed. (A) Nitrate MBGs. (B) Chloride MBGs. The outstanding concordance of calculated (in red) and experimental (in black) spectra confirms the goodness of the fitting. (For interpretation of the references to colour in this figure legend, the reader is referred to the Web version of this article.)

Europe PMC Funders Author Manuscripts

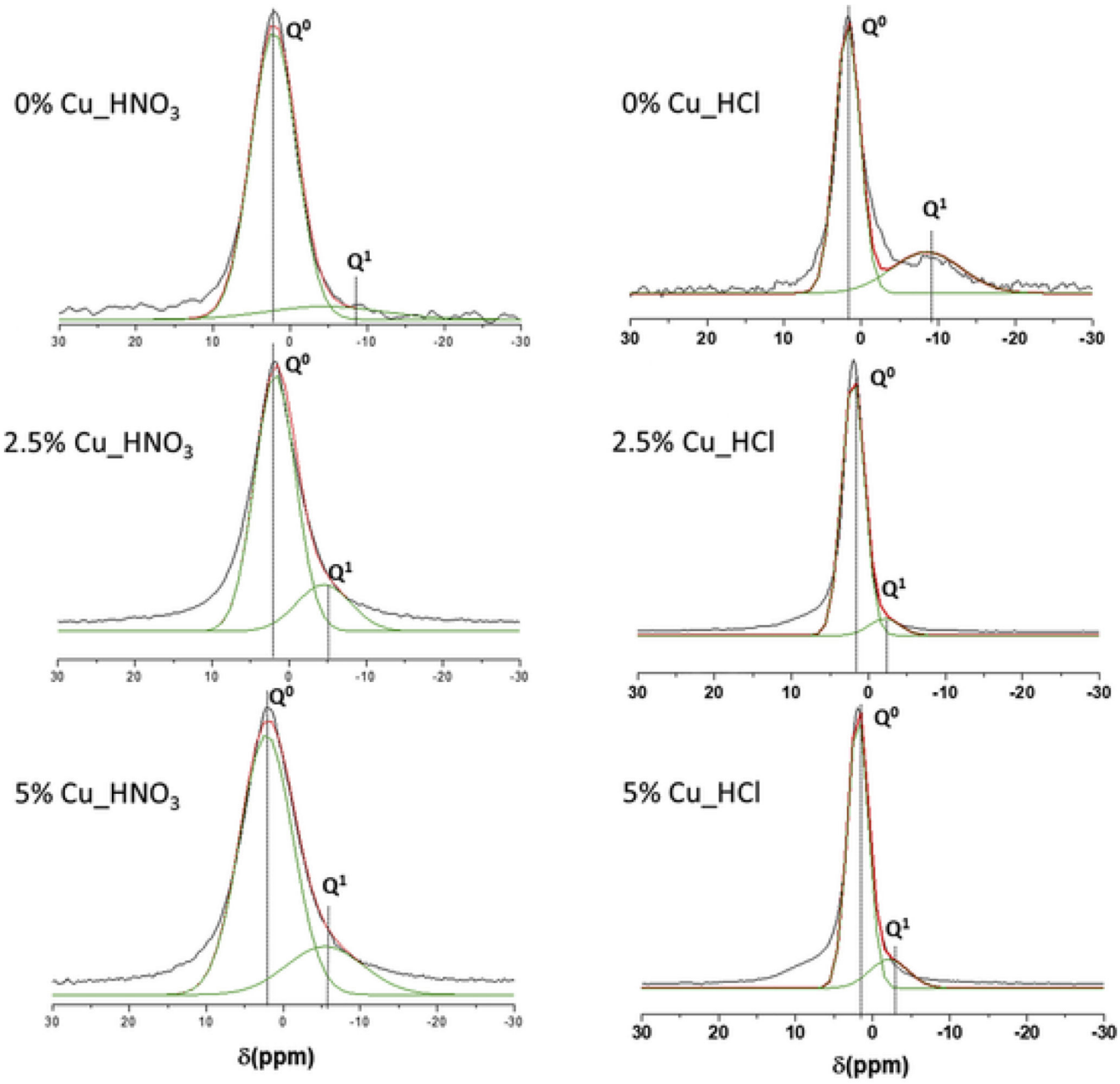

Fig. 4.

Solid-state ^{31}P single-pulse MAS-NMR spectra of MBGs. Q^0 and Q^1, obtained by Gaussian line-shape deconvolution, are displayed in green. Left: Nitrate series. Right: Chloride series. The outstanding concordance of calculated (in red) and experimental (in black) spectra confirms the goodness of the fitting. (For interpretation of the references to colour in this figure legend, the reader is referred to the Web version of this article.)

Europe PMC Funders Author Manuscripts

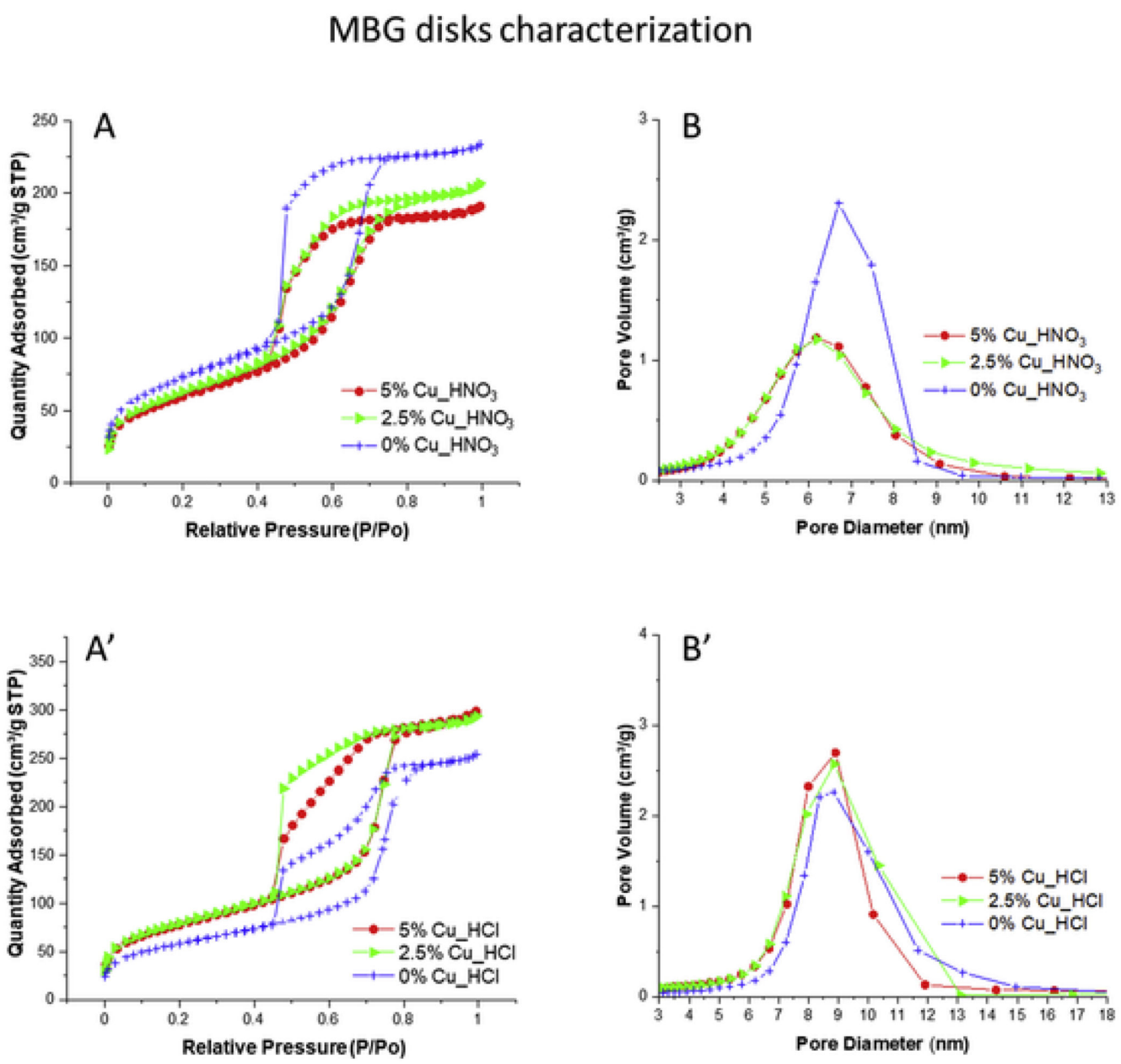

Fig. 5.

N_2-adsorption results showing the isotherms (A, A′) and pore size distributions (B, B′) of nitrate and chloride MBGs after be compacted into disks.

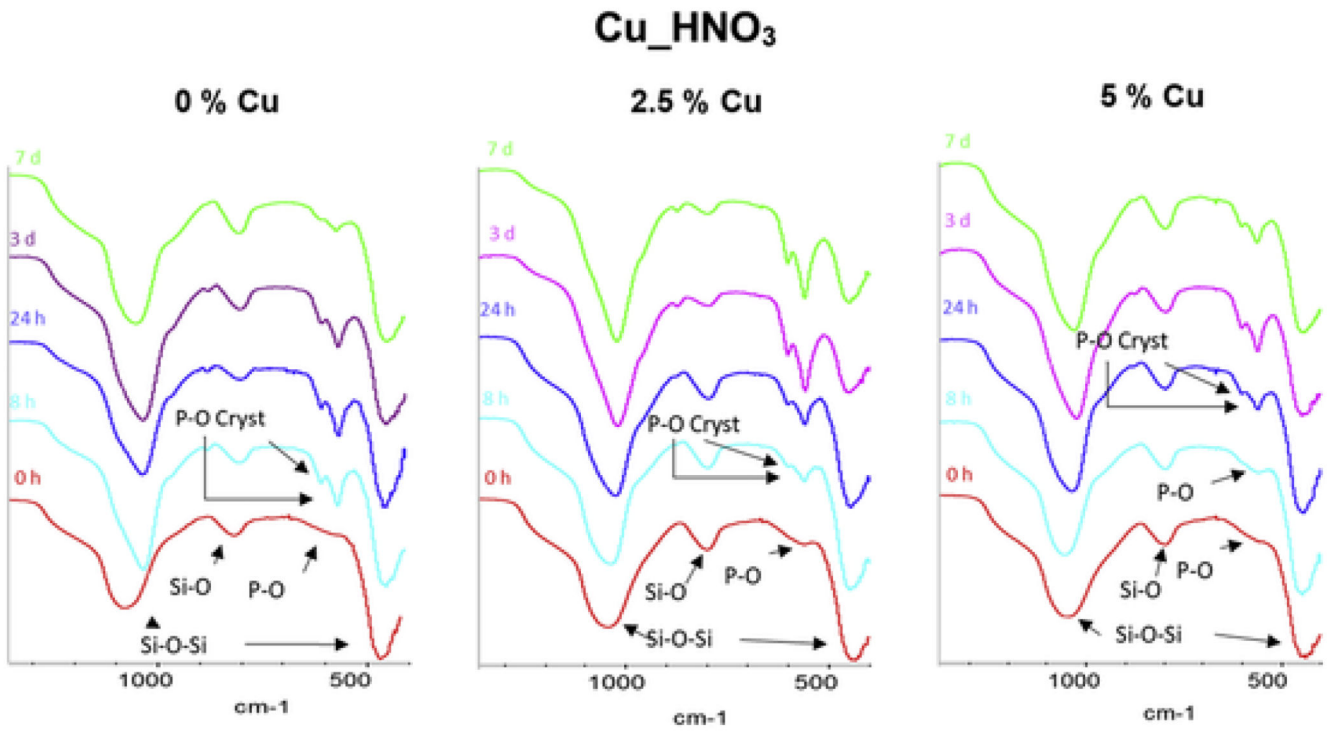

Fig. 6.

FTIR spectra of nitrate series before and after 8 h, 24 h, 3 d and 7 d of immersion in SBF. Arrows highlight the most significant bands of Si–O and P–O in the spectra. Of interest are the bands of phosphate in a crystalline environment, labeled as P–O Cryst.

Europe PMC Funders Author Manuscripts

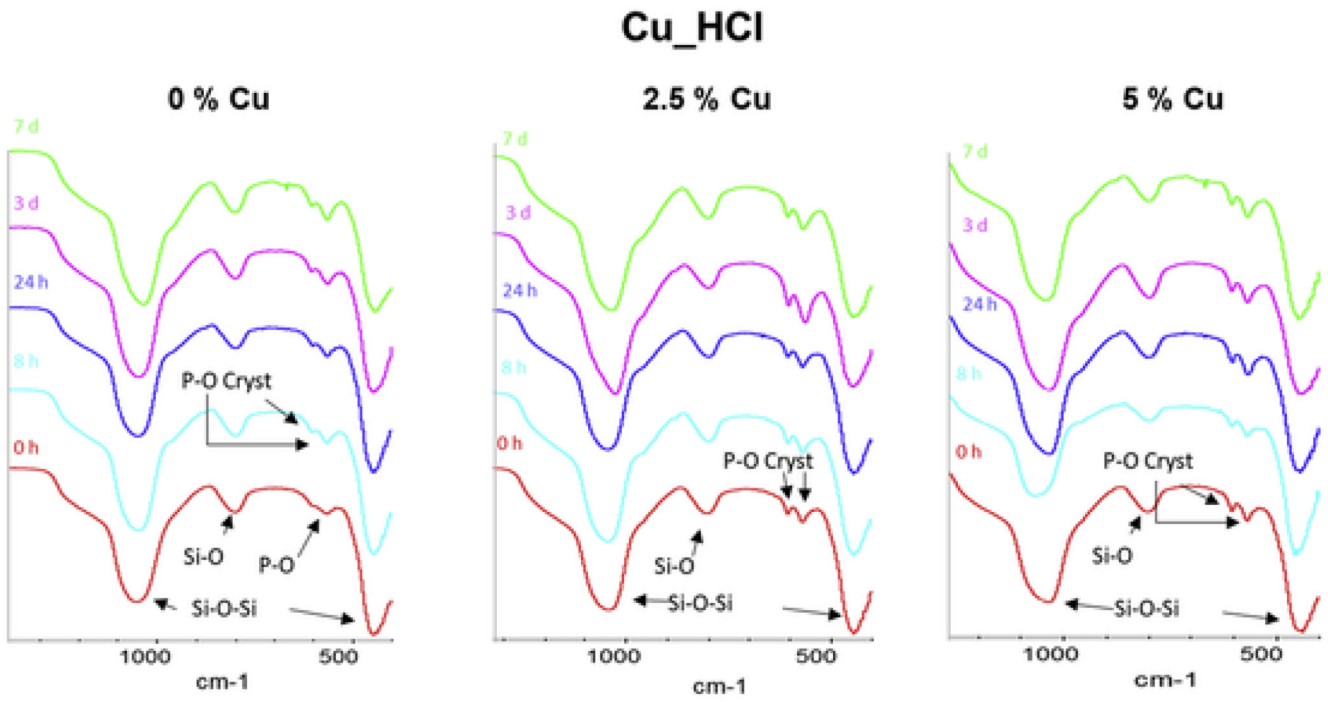

Fig. 7.

FTIR spectra of chloride series before and after 8 h, 24 h, 3 d and 7 d of immersion in SBF. Arrows highlight the most significant bands of Si–O and P–O in the spectra. Of interest are the bands of phosphate in a crystalline environment, labeled as P–O Cryst.

Europe PMC Funders Author Manuscripts

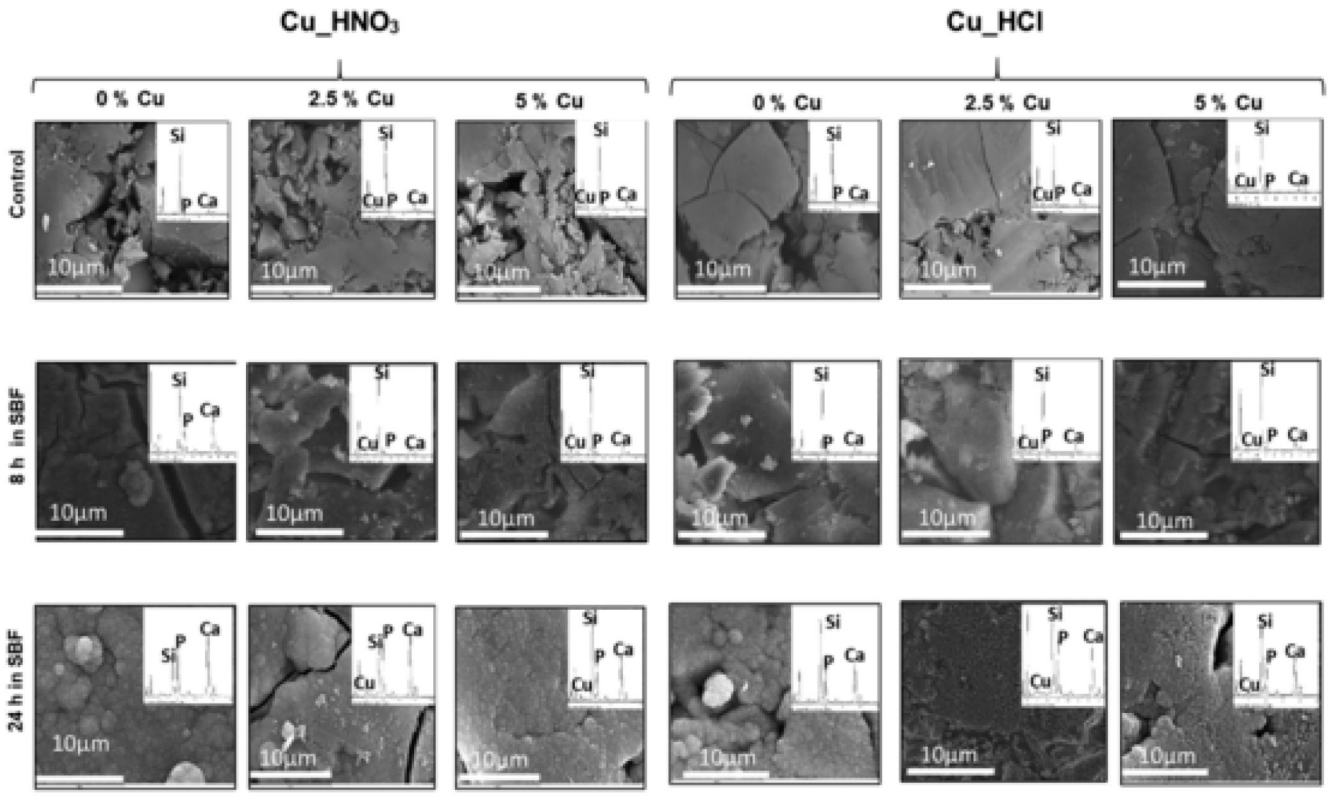

Fig. 8.

SEM images of the disks surface before and after 8 and 24 h of immersion in SBF. Each image includes their respective EDS spectrum.

Europe PMC Funders Author Manuscripts

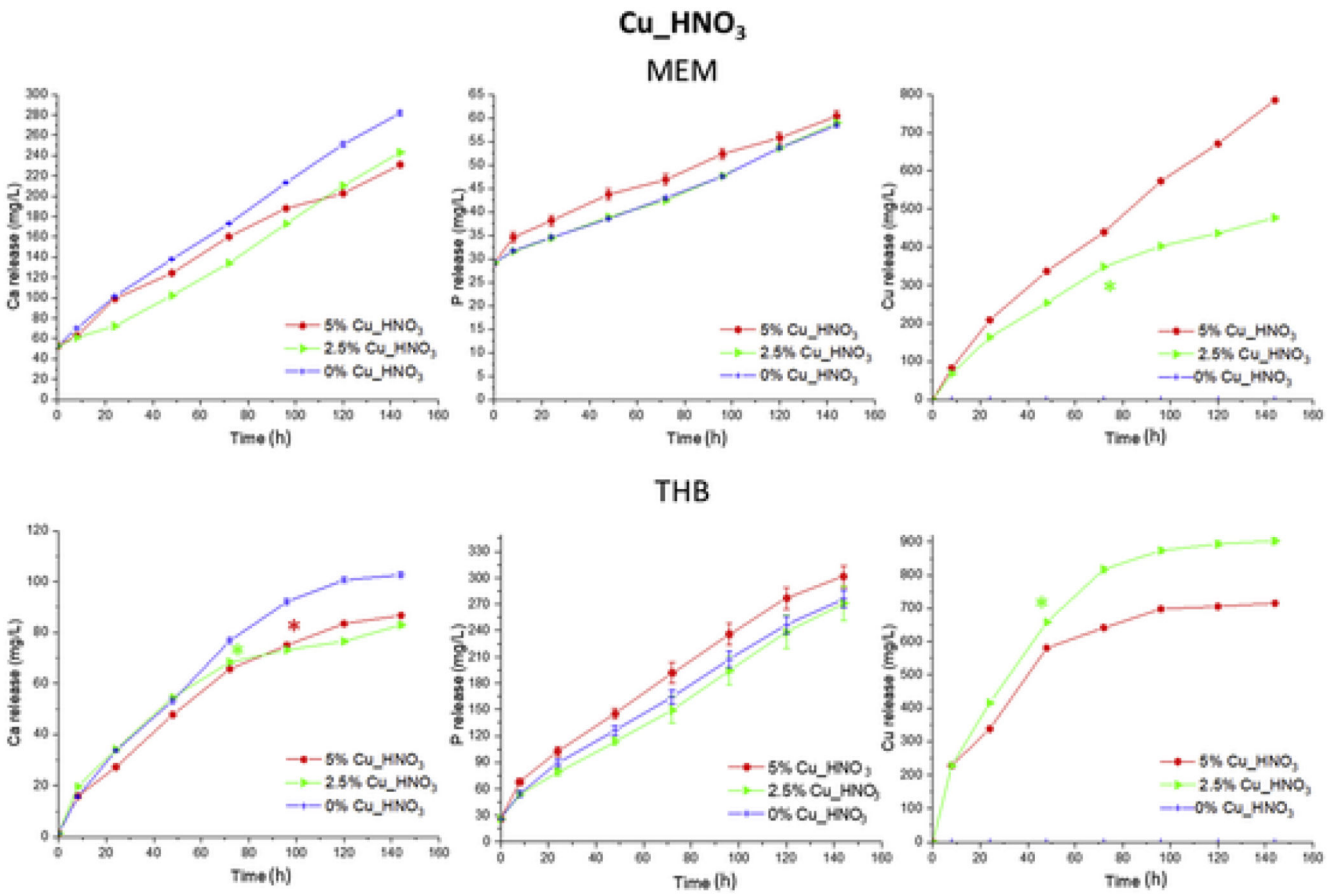

Fig. 9.

Cumulative release of calcium, phosphorous and copper from nitrate series as a function of the time soaked in MEM and THB. The significant differences are marked with the symbol * in the time from which a p-value>0.05 was obtained with respect to the sample without copper, except for the measurement of copper.

Europe PMC Funders Author Manuscripts

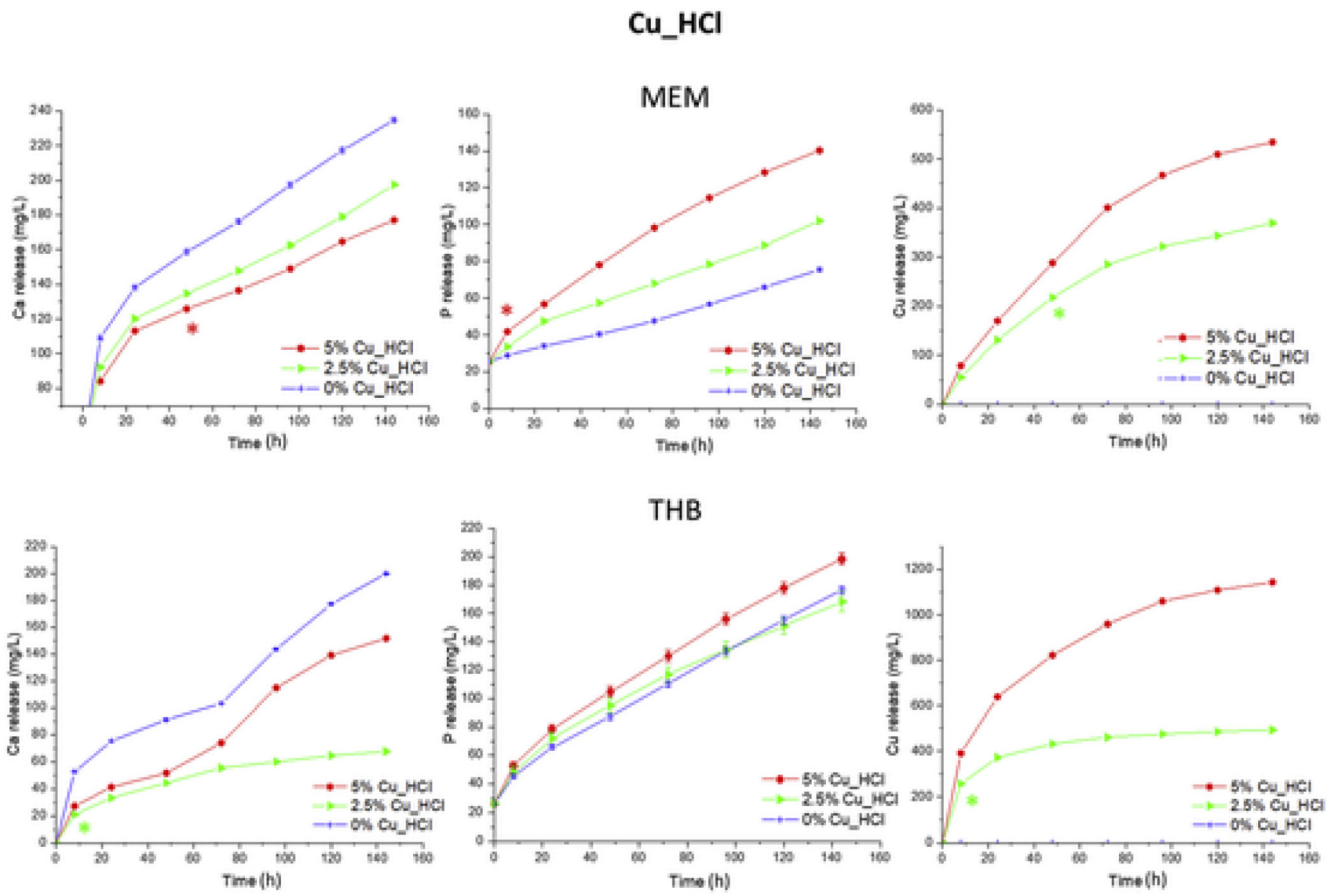

Fig. 10.

Cumulative release of calcium, phosphorous and copper from chloride batch as a function of the time soaked in MEM and THB. The significant differences are marked with the symbol * in the time from which a p-value>0.05 was obtained with respect to the sample without copper, except for the measurement of copper.

Europe PMC Funders Author Manuscripts

Table 1

Amounts of reactants used in the synthesis of MBG series (F127: Pluronic® F127; Et–OH: ethanol; TEOS: tetraethyl orthosilicate, TEP: triethyl phosphate).

Sample	F127 (g)	Et–OH (mL)	H_2O (mL)	HNO_3 1 M (mL)	HCl 1M (mL)	TEOS (mL)	TEP (mL)	Ca $(NO_3)_2 \cdot 4H_2O$ (g)	Cu $(NO3)_2 \cdot 2.5H_2O$ (g)	$CaCl_2 \cdot 2H_20$ (g)	$CuCl_2$ (g)
0% Cu_HNO 3	6.5	56.2	6.46	5.45	¬	12.4	1.12	1.56	0	¬	¬
2.5% Cu_HNO 3	6.5	56.2	6.46	5.45	¬	12.2	1.12	1.56	0.384	¬	¬
5% Cu_HNO 3	6.5	56.2	6.46	5.45	¬	11.9	1.12	1.56	0.768	¬	¬
0% Cu_HCl	6.5	56.2	6.46	¬	4.26	12.4	1.07	¬	¬	0.822	0
2.5% Cu_HCl	6.5	56.2	6.46	¬	4.26	11.7	1.07	¬	¬	0.822	0.212
5% Cu_HCl	6.5	56.2	6.46	¬	4.26	11.4	1.07	¬	¬	0.822	0.425

Europe PMC Funders Author Manuscripts

Table 2

Textural parameters of MBGs as powders and after being processed into disks (S_{BET}: BET surface area, V_P: pore volume and D_P pore diameter). MBGs composition (atom-%) determined by EDS is also included. Standard deviations were omitted for simplifcation, but they were for all the values inferior to 7%.

Sample	Powders			Disks			Composition (atomic-%)			
	$S_{BET}(m^2g^{-1})$	V_p (cm^3g^{-1})	D_P (nm)	$S_{BET}(m^2g^{-1})$	V_p (cm^3g^{-1})	D_P (nm)	Si	P	Ca	Cu
0% Cu_HNO 3	301	0.41	6.7	261	0.35	6.7	89.6	2.2	8.2	0
2.5% Cu_HNO 3	275	0.38	6.2	228	0.31	6.2	85.8	4.4	7.2	2.7
5% Cu_HNO 3	261	0.35	6.1	216	0.28	6.2	82.3	2.4	8.3	5.3
0% Cu_HCl	218	0.40	8.8	211	0.38	8.8	85.4	7.1	7.5	0
2.5% Cu_HCl	295	0.46	8.4	288	0.44	8.8	80.6	10.2	7.6	1.6
5% Cu_HCl	290	0.47	8.8	282	0.45	8.9	80.7	8.4	8.6	2.4

Europe PMC Funders Author Manuscripts

Table 3

Position of the sharp (10) maxima observed in the SA-XRD patterns of MBGs. In each case, the interplanar spacing (d) and the calculated unit cell parameter (a_o) are also included.

Sample	(10) maximum (θ)	Interplanar spacing d(10) (nm)	a_0 (nm)
0% Cu_HNO $_3$	0.98	9.0	10.4
2.5% Cu_HNO $_3$	0.98	9.0	10.4
5% Cu_HNO $_3$	1.04	8.5	9.8
0% Cu_HCl	0.88	10.0	11.6
2.5% Cu_HCl	0.86	10.3	11.9
5% Cu_HCl	0.88	10.0	10.0

Table 4

Chemical shifts (CS) and relative peak areas of MBGs obtained by ^{29}Si and ^{31}P NMR. For each MBG, the silica network connectivity <Q^n> is also included.

Sample	^{29}Si							^{31}P			
	Q^4		Q^3		Q^2			Q^1		Q^0	
	CS ppm	Area [a] (%)	CS ppm	Area [a] (%)	CS ppm	Area [a] (%)	<Q^n>	CS ppm	Area [a] (%)	CS ppm	Area [a] (%)
0% Cu_HNO$_3$	−112	72.0	−103	27.5	−97	0.5	3.71	−4.5	10.4	2.1	89.5
2.5% Cu_HNO$_3$	−112	67.6	−102	31.2	−96	1.0	3.66	−4.5	19.4	1.9	80.6
5% Cu_HNO$_3$	−112	64.1	−106	33.9	−95	2.0	3.62	−5.4	21.2	2.2	78.8
0% Cu_HC1	−111	84.1	−102	12.0	−95	3.8	3.8	−8.5	29.9	1.8	70.0
2.5% Cu_HCl	−111	81.9	−102	12.7	−98	5.3	3.76	−2.1	8.3	1.9	91.7
5% Cu_HC1	−112	64.6	−105	30.4	−98	4.9	3.59	−2.1	9.6	1.9	90.4

[a]Areas of the Q^nunits were calculated by Gaussian deconvolution. The relative populations were expressed as %.